# Architecture and Devices for Silicon Photonic Switching in Wavelength, Polarization and Mode

Yong Zhang ⓘ , *Member, IEEE, Member, OSA*, Ruihuan Zhang, Qingming Zhu ⓘ, Yuan Yuan,
and Yikai Su ⓘ, *Senior Member, IEEE*

*(Invited Paper)*

*Abstract*—**Switching can be performed with multiple physical dimensions of an optical signal. Previously optical switching was mainly focused in the wavelength domain. In this paper we discuss the general architecture of integrated silicon photonic switches by exploiting multi-dimensions in wavelength, polarization, and mode. To route a data channel from one input port to an arbitrary output port in a network node, three basic functions are required: de-multiplexing, switching, and multiplexing. The multiplexing and de-multiplexing processes can be realized in any one physical dimension. The capacity of a switch can be effectively scaled by using joint physical dimensions. As two examples, we first present a wavelength switch based on dual-nanobeam cavities with high quality factors, a low power consumption, and a compact footprint. We then propose a design of a mode-polarization-wavelength selective switch by leveraging three physical dimensions, and experimentally demonstrate the building blocks and key functionalities.**

*Index Terms*—**Demultiplexing, laser modes, multiplexing, optical polarization, optical switches, silicon photonics, wavelength division multiplexing.**

## I. INTRODUCTION

**T**HE total capacity of fiber optic networks has grown exponentially for decades [1]. To meet the demand for the rapidly increasing bandwidth, multiple physical dimensions of an optical carrier have been exploited for modulation or multiplexing, including time, wavelength, polarization, amplitude and phase. These techniques correspond to time division multiplexing (TDM), wavelength division multiplexing (WDM), polarization division multiplexing (PDM), and quadrature amplitude and phase (QAM) modulation, respectively. Recently, mode-division multiplexing (MDM) was studied to further increase the capacity by using the spatial modes of fibers [2] or waveguides [3]–[5].

The authors are with the State Key Laboratory of Advanced Optical Communication Systems and Networks, Department of Electronic Engineering, Shanghai Jiao Tong University, Shanghai 200240, China (e-mail: yongzhang@ sjtu.edu.cn; ruihuan@sjtu.edu.cn; zhuqm@sjtu.edu.cn; yyuantsoi@sjtu.edu.cn; yikaisu@sjtu.edu.cn).

In reconfigurable optical networks and data centers, switching of an incoming data stream to an arbitrary output port in a network node is a basic requirement. In general, there are two approaches towards optical switching: free space and integrated schemes. Recently, silicon photonic integrated switches have attracted much attention for their advantages of compact footprint due to the high refractive index of the silicon waveguide, low power consumption originating from the small mode volume of light, and compatibility with CMOS fabrication processes. In [6], we reviewed our progress on three silicon thermo-optic (TO) chips for optical switching in wavelength, polarization and mode. These devices included 1) a $2 \times 2$ wavelength switch using two cascaded nanobeam cavities with a low switching power of 0.16 mW; 2) a $2 \times 2$ wavelength switch using two nanobeam resonators in a parallel Mach-Zehnder interferometer (MZI) configuration with a reduced footprint of 38 $\mu$m $\times$ 84 $\mu$m; 3) a $2 \times 2$ mode and polarization selective switch.

In this paper, we extend our study on the switching architecture and also present two new switching chips. Our results consist of: 1) a general architecture for optical switching in arbitrary physical dimensions; 2) an improved dual-nanobeam wavelength switch with high quality factors (Q-factors), a lower power consumption, and a compact footprint; 3) a design of a mode-polarization-wavelength selective switch that leverages three physical dimensions, and an experimental demonstration of the building blocks and key functionalities.

The paper is organized as follows. Section II discusses the general switching architecture with any physical dimension. Section III demonstrates a compact one-dimensional wavelength switch based on nanobeam resonators in an MZI configuration with higher Q-factors and lower power consumption relative to our previous work [7]. In Section IV, we briefly review two-dimensional switches. In Section V, we present a design of a new three-dimensional switch in mode, polarization and wavelength, and provide experimental results on the building blocks and key functionalities. Finally, Section VI summarizes the work.

## II. GENERAL ARCHITECTURE FOR OPTICAL SWITCHING IN DIFFERENT PHYSICAL DIMENSIONS

Switching is a process that can route a data channel from one input port to an arbitrary output port. To realize this, a selected
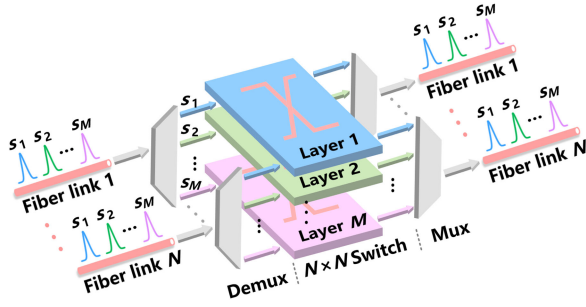
Fig. 1.    A general architecture for optical switching in one physical dimension (wavelength, polarization or mode).
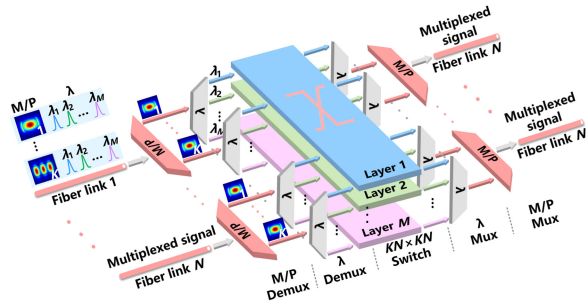


Fig. 2.    A general architecture for optical switching in multiple dimensions (joint wavelength, polarization and mode). M/P: mode/polarization. λ: wavelength.



Fig. 3.    A Benes network built on $2 \times 2$ switching units.

channel needs to be de-multiplexed from an input fiber, directed to a destined output port, and then combined with other channels before being sent to an output fiber. Therefore, three basic functions are employed in a network node: de-multiplexing, switching, and multiplexing, as shown in Fig. 1. The multiplexing and de-multiplexing processes can be performed in any one physical dimension, denoted as $s$. Equation (1) shows an optical carrier with possible physical parameters to manipulate [8]:

$$\overrightarrow{E\left(x, y, z, t\right)} = \overrightarrow{e} \cdot F\left(x, y, t\right) \cdot |A\left(z, t\right)| \cdot \Phi\left(z, t\right)$$
$$\cdot \exp\left[j\left(wt - kz\right) + \varphi\right], \qquad (1)$$

where $\overrightarrow{E}$ is the optical field, $x$, $y$, $z$ are the space coordinates, $t$ is the time, $\overrightarrow{e}$, $F$, $|A|$, $\Phi$ represents the polarization state, mode, amplitude, phase of the optical carrier, respectively, $w$ is the frequency, $k$ is the wavenumber, and $\varphi$ is the initial phase of the carrier. In Fig. 1, between the de-multiplexers and the multiplexers, the switching function is implemented on different layers, which operate with orthogonal channels in the same physical dimension. Therefore, the switching elements on each layer can take a small fraction of the available operation range in the corresponding physical domain. Particularly, in the case of the WDM switch, the switching elements can be narrowband and thus resonator devices may be employed. Wavelength locking of the resonators to the input signals is needed. On each switching layer, the devices are of the same design parameters.

To increase the switching capacity, multiple physical dimensions can be utilized. Fig. 2 shows an architecture for optical switching in wavelength, polarization and mode. The input
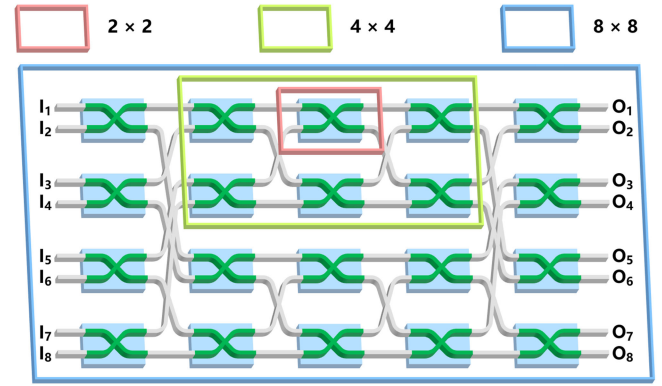
fibers carry data signals multiplexed in multi-dimensions. These signals are first separated in mode and polarization by the de-multiplexers denoted as M/P demux's, and then followed by the wavelength de-multiplexers (λ demux's). It can be seen in Fig. 2 that the number of the switching layers remains the same as that in Fig. 1 determined by the number of the wavelengths, while the port count of each switching layer is increased by a factor of the mode and polarization channel number. Therefore, it is important to build high-radix $N \times N$ switches. Note that the mode de-multiplexers also convert the input high order modes to fundamental modes before the switches. Therefore, all the output signals of the mode/polarization demultiplexers can have the same polarization of a fundamental mode if polarization rotators are used. Switching between modes provides flexibility in the switch architecture design, at the cost of the increased complexity [9]. The topologically separated switching layers can be physically placed on the same plane in a practical implementation, as will be discussed in Section V.

A switch is considered to be non-blocking if each input signal can be routed to any unused output port, otherwise it is a blocking switch [10]. Typically, non-blocking switches are desired for most applications, since they can greatly reduce the complexities of resource allocating and signal routing, and improve the network utilization [10], [11]. However, in a large-scale switching application, a non-blocking switch may exhibit much higher complexities in device design and fabrication than a blocking switch [12]. In such a scenario, the blocking topology may be used for a switch with a large port count to interconnect thousands of servers/pods or beyond. In a $N \times N$ switch, $2 \times 2$ crossbar switches are the basic building blocks on the switching layers. Diverse switching topologies have been proposed to construct a non-blocking large scale switch from the $1 \times 2$ or $2 \times 2$ switching units [13], e.g., crosspoint, Benes, Switch-and-select, Banyan, and etc. Fig. 3 illustrates the process to build an $8 \times 8$ Benes network by cascading the $2 \times 2$ crossbar switching units.

The capacity of a multi-dimensional switch depends on the number of the available orthogonal channels in the physical dimensions. WDM can provide tens of data channels (e.g., 40, 80 or more) in the C band. PDM offers only two orthogonal channels. Current state-of-the-art MDM technologies have achieved 15 modes in fibers [14] or more than 10 single-polarization

modes on silicon chips [15]. Therefore, combining WDM with MDM enables effective scaling of the capacity if the crosstalk issue can be well resolved.

Another issue of consideration is the power consumption. In principle, optical switching in integrated waveguides without mechanical movement is essentially a modulation process. Firstly, a phase shift in a waveguide is induced by the refractive index change by modulation, either through TO or electro-optic (EO) effect. Then, the light with the phase shift interferes with another modulated light or a reference light, leading to a change of the output port. Thus, to lower the power consumption, it is desired to: 1) reduce the power to achieve a given phase shift (e.g., $\pi$); 2) switch a light to a different output port with a minimum phase shift by using, e.g., a resonator structure. In [16], a detailed study was carried out to reveal the power consumptions of EO modulation devices, and it was found that the mode volume of the EO device plays an important role. From this aspect, it is of high interest to investigate a resonator device with tight confinement of the light in an ultra-small mode volume, as such a device satisfies the above two requirements simultaneously.

Other factors such as loss, crosstalk, response time, scalability and etc. of the switch should be taken into account towards practical implementations. Though this paper focuses on the fundamental study of optical switching in different dimensions. In the following sections, we will demonstrate an improved nanobeam-resonator based wavelength switch with a low power consumption, and report a proof-of-concept experiment of a mode-polarization-wavelength selective switch. Although only thermal tuning approach is demonstrated, these switches can be combined with EO tuning to enable fast switching speeds.

## III. COMPACT ONE-DIMENSIONAL $2 \times 2$ WAVELENGTH SWITCH

In the past few years, switches based on photonic crystals have emerged due to the compact footprints and low power dissipations [17]–[23]. The enhanced interaction between the light and matter in a standing-wave photonic-crystal resonator makes it a promising candidate to reduce the device size and improve the tuning efficiency [24]–[27]. Photonic-crystal nanobeam (PCN) is a one-dimensional (1D) photonic crystal, which consists of a series of circular holes to form a wavelength-scale Fabry-Perot (F-P) cavity [21]. In a silicon PCN cavity, photons are strongly confined within a small volume ($\sim$0.2 $\mu m^3$), and the Q-factor of the cavity is high. These properties lead to a high tuning efficiency and a low tuning power of the PCN based device. In our previous work, we demonstrated a $2 \times 2$ TO switch based on a dual-nanobeam MZI structure [7]. The heating powers for achieving the cross and bar states were $\sim$2.66 mW and $\sim$2.36 mW, respectively, which were mainly determined by the relatively low Q-factors ($\sim$2000) of the two PCN cavities. Further optimizations of the device performances are needed.

Reducing the cavity loss is an effective method to improve the Q-factor of the PCN. It can be realized by increasing the hole number and the hole radius of the PCN to maintain the phase matching between the silicon waveguide mode and the PCN
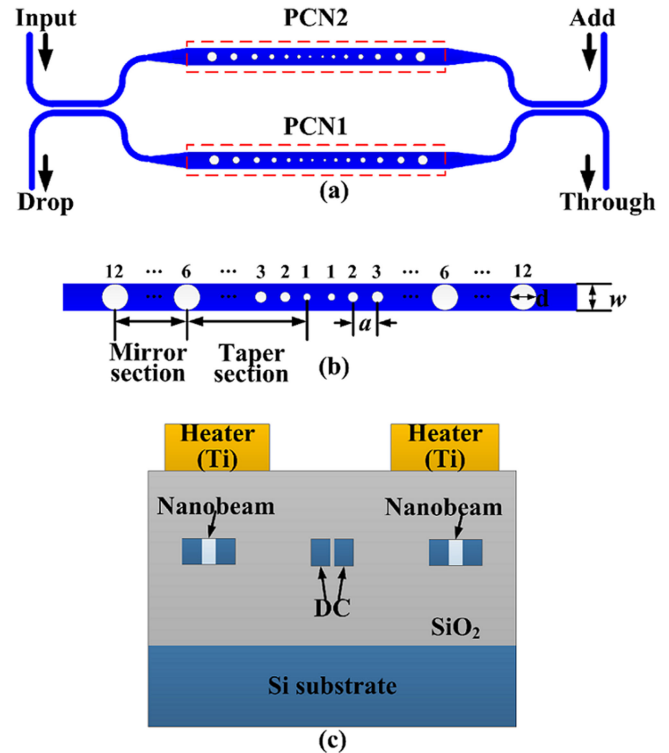


Fig. 4. (a) Schematic diagram of the $2 \times 2$ TO switch based on the dual-nanobeam MZI. (b) Structure of the PCN. (c) Cross section of the configuration.

fundamental Bloch mode, and thus lowering the cavity radiation loss. However, the cavity mode volume increases linearly with this change due to the enlarged dielectric profile in the middle plane of the cavity [27]. In addition, the width of the PCN should be optimized with the hole radius to achieve a high effective index of the cavity mode, thus reducing the in-plane radiation loss of the cavity. Here, we design a PCN cavity with a relatively high Q-factor and a small mode volume by properly increasing the hole number and carefully optimizing the hole radius and the period simultaneously. The designed PCN contains 24 etched holes with varying hole radii and periods. The width of the waveguide is optimized to be 530 nm. To experimentally verify the design, we fabricated a $2 \times 2$ TO MZI switch based on the PCN cavities. Only 0.24 mW is needed to change the switch states with a Q-factor of 13000. The overall tuning efficiency of the switch is 0.66 nm/mW. The insertion losses (ILs) and crosstalk (CT) of the TO switch are measured as IL (bar) = 0.21 dB, IL (cross) = 1.5 dB, CT (bar) = –15 dB and CT (cross) = –16.8 dB at the cross and bar states, respectively. The footprint of the device is 15 $\mu$m $\times$ 75 $\mu$m.

The schematic configuration of the proposed switch is shown in Fig. 4(a). Two identical PCNs are embedded in the two arms of the MZI switch, respectively. Two 3-dB directional couplers (DCs) are placed symmetrically at the input and output ports, and connected to the MZI arms as beam splitters. The PCNs perform the wavelength de-multiplexing while the MZI functions as the switch. In order to keep the compact footprint of the device, the widths, lengths and gaps of the 3-dB DCs are designed to be

450 nm, 11.5 $\mu$m and 200 nm, respectively. The structure of the PCN is illustrated in Fig. 4(b). It contains 24 etched holes to form a F-P cavity which is symmetric with respect to its center. Each side of the F-P cavity includes one mirror section and one taper section to realize a phase matching between the waveguide mode and the photonic crystal fundamental Bloch mode, in order to reduce the cavity scattering loss [24]. Considering the device performance and the fabrication limitation, the hole radii of two sections are optimized as: $r(n) = T[p + 0.02(n-1)]$, ($n = 1$, …, 6), $r(n) = T[p + 0.02 \times (6-1)]$, ($n = 7$, …, 12). The ratio of the radius to the period $T$ is 0.26, while the smallest period $p$ is 0.29 $\mu$m. Each PCN acts as a F-P cavity. The two off-resonant lights in the two arms of the MZI are reflected to the 3-dB DC at the input ports. The two lights having the same phases are coupled in the 3-dB DC, combined and output to the drop port. On the other hand, the two resonant lights in the two arms are combined and transmitted to the through port. If the two arms of the MZI are heated, the two resonances shift simultaneously, thus the lights at the drop port and the through port switch their paths.

The diameters of the holes are designed as $d_1 = 150$ nm, $d_2 = 162$ nm, $d_3 = 172$ nm, $d_4 = 182$ nm, $d_5 = 192$ nm, $d_6 = 202$ nm, respectively. The corresponding intervals are $a_1 = 134$ nm, $a_2 = 143$ nm, $a_3 = 153$ nm, $a_4 = 163$ nm, $a_5 = 173$ nm, respectively. In addition, the spacing between the two central holes is designed as $a_0 = 134$ nm to reduce the mode volume of the cavity. Other holes are distributed symmetrically next to the taper holes to form the mirror sections. All these holes have the same diameters of $d_i = 202$ nm ($i = 7$, …, 12) and the same intervals of $a_i = 188$ nm ($i = 6, 7$, …, 11) as the reflection mirrors. The waveguide width of the PCN is optimized to be 530 nm to reduce the in-plane radiation loss. Four 5-$\mu$m-long tapers are used to connect the 450-nm-wide waveguides with the 530-nm-wide PCN waveguides at the front and rear ports to minimize the scattering losses in the waveguides. Fig. 4(c) shows the cross section of the configuration.

A simulation was performed based on the 2.5D variational finite-difference-time-domain (FDTD) to achieve a time-efficient and accurate calculation process. The calculated electric field intensity distribution is shown in Fig. 5(a). It can be seen that the power of the light is confined within a small area in the center with a length of about 3 $\mu$m. The Q-factor of the PCN cavity is $\sim 10^4$, which leads to a low tuning power. The mode volume of the cavity is calculated to be 0.211 $\mu$m$^3$, which enables a high thermal tuning efficiency. The transmission spectra of the switch are calculated utilizing the transfer matrix method. Simulated transmission results are depicted in Fig. 5(b). Note that the transmission spectra present a deep notch at the drop port and a sharp peak at the through port at the wavelength of 1537 nm, respectively.

The proposed switch was fabricated on a silicon-on-insulator (SOI) wafer, with a 220-nm-thick top silicon layer and a 3-$\mu$m-thick buried silica layer. The silicon waveguides and PCNs were fabricated by E-beam lithography (EBL) (Vistec EBPG 5200$^+$) and inductively coupled plasma (ICP) etching process. The PCNs were etched in the two arms of the MZI. A 1.5-$\mu$m-thick silica layer was deposited over the waveguides by plasma
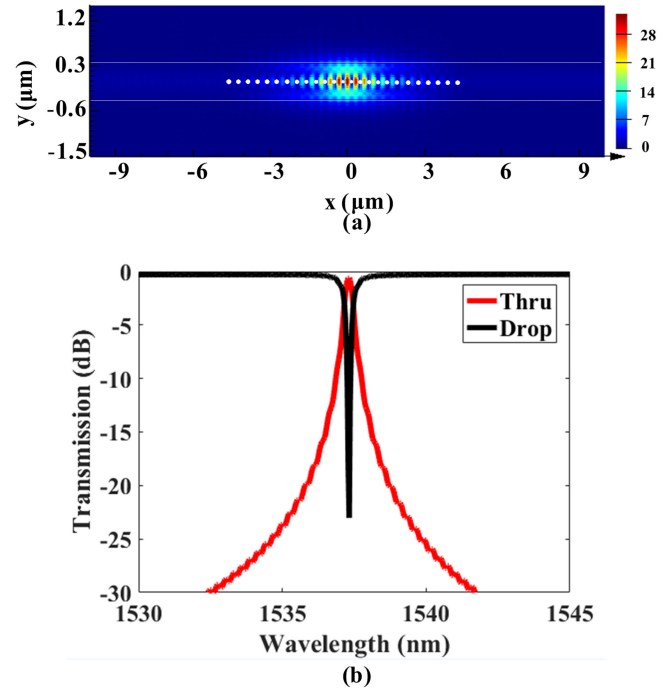


Fig. 5. (a) Simulated electric field distribution in PCN. (b) Simulated transmission spectra of the switch.
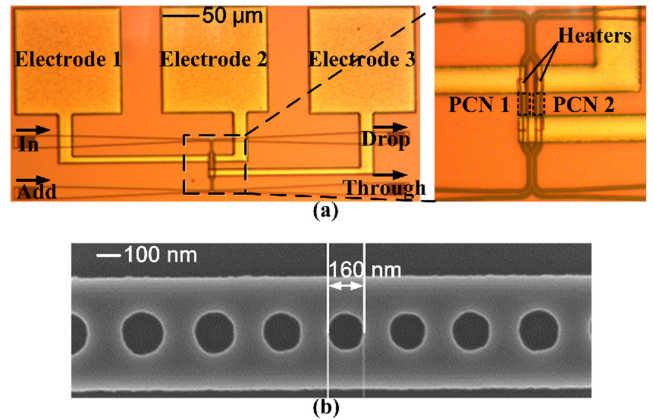


Fig. 6. (a) Micrograph of the proposed switch. The inset is the zoom-in view of the dual-nanobeam based MZI. (b) SEM image of the fabricated PCN.

enhanced chemical vapor deposition (PECVD) for protection. Two heaters were sputtered on the silica layer above the PCNs to implement the thermal tuning of the device. The heaters were fabricated with 2-$\mu$m-thick aluminum and 100-nm-thick titanium. Three pads were connected to the heaters as the electrodes for the probes. Both the heaters and the electrodes were fabricated by lift-off processes. The picture of the fabricated device is shown in Fig. 6(a). The lengths of the metal electrodes and heaters are 150 $\mu$m and 20 $\mu$m, respectively. Four vertical coupling gratings for TE polarization were placed at the two input ports and two output ports to couple the light into and out of the device. Fig. 6(b) shows the scanning electron microscope (SEM) image of the fabricated PCN.
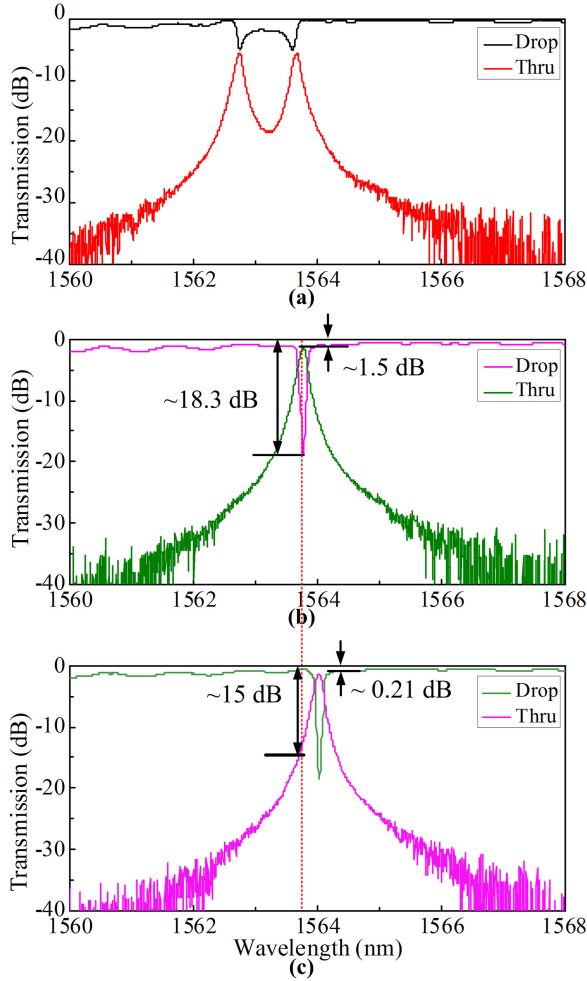
Fig. 7. (a) Initial transmission spectra at drop port and through port. (b) Transmission spectra of the fabricated switch at the cross state. (c) Transmission spectra of the fabricated switch at the bar state. Note that the transmission spectra are normalized to a reference waveguide.
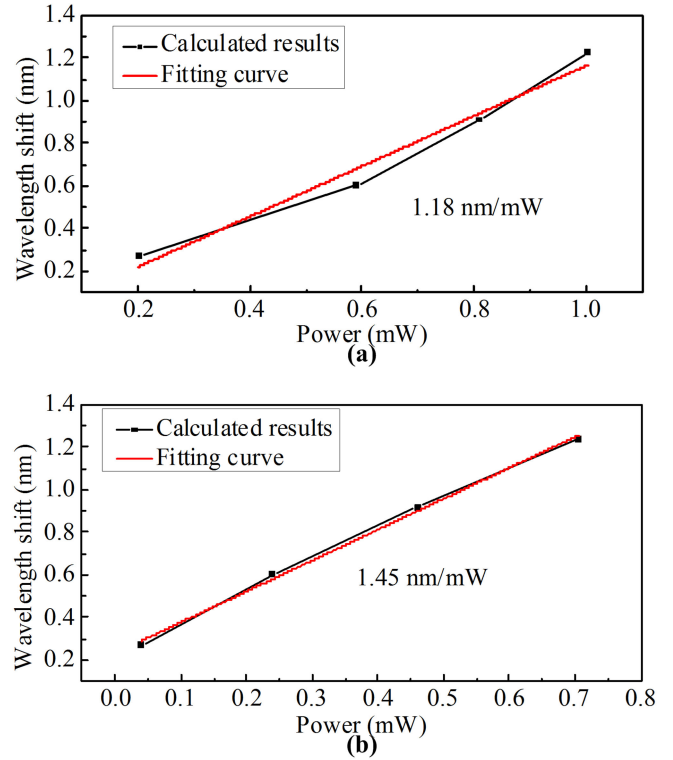


Fig. 8. (a) Fitting curve of the PCN1 resonance wavelength shift against the applied power. (b) Fitting curve of the PCN2 resonance wavelength shift against the applied power.

The transmission spectra of the fabricated switch are depicted in Fig. 7. Fig. 7(a) shows the transmission spectra at the drop port and the through port without applying external electric power to the heaters. The initial resonance wavelengths of the two nanobeam cavities are separated due to the fabrication errors, which are 1562.74 nm (arm1) and 1563.77 nm (arm2), respectively. The shorter resonance wavelength should be red-shifted to align with the longer one before switch tuning. About 1.05 mW of electric power is applied for the alignment. Note that this power can be minimized by reducing the fabrication errors. Once the two resonance wavelengths are aligned at 1563.77 nm (Fig. 7(b)), the switch works at the cross state. The CT at the drop port is measured to be −16.8 dB, and the IL at the through port is 1.5 dB. The insertion loss can be reduced by further optimizing the design parameters and improving the fabrication processes.

To achieve the bar state of the switch, a thermal tuning power of 0.24 mW is needed to shift both of the resonance wavelengths from 1563.77 nm to 1563.93 nm [Fig. 7(c)] simultaneously, which corresponds to a CT of −15 dB at the through port, thus most of the light outputs from the drop port at the previous resonance wavelength of 1563.77 nm. The switch changes from cross state to bar state with only 0.24 mW power consumption. Here, we define the switching power as the required power that realizes the switching of the state after the resonance wavelengths of the two PCNs are aligned. The CT at the through port is −15 dB, and the IL at the drop port is 0.21 dB at the bar state. The full width at half maximum (FWHM) of the transmission spectrum at the through port is 0.121 nm (3-dB bandwidth of 15 GHz) with a Q-factor of 13000. In practical applications, the bandwidth can be designed to be wider, while maintaining a high extinction ratio and a low IL. Here we focus on achieving a high Q-factor switch with a low switching power. The crosstalk may limit the performance of the switch. While previous study showed that an inter-channel crosstalk of $< -15$ dB can satisfy error-free operation with most modulation formats, higher crosstalk suppression is desired by using, e.g., cascaded resonators.

Furthermore, to obtain the thermal tuning efficiency of the switch, different external powers were applied to the heaters. The two PCNs were thermally tuned to ensure the synchronous shifts of the two resonance wavelengths. The tuning efficiencies of PCN1 and PCN2 are 1.18 nm/mW and 1.45 nm/mW, respectively, as shown in Fig. 8.

Fig. 9(a) provides more detailed transmission spectra with different total powers of $P_1 = 0$, $P_2 = 0.24$, $P_3 = 0.83$, $P_4 = 1.27$, $P_5 = 1.71$ mW. The wavelength-power relation is plotted in Fig. 9(b). The overall tuning efficiency of the device including the two PCNs is 0.66 nm/mW.
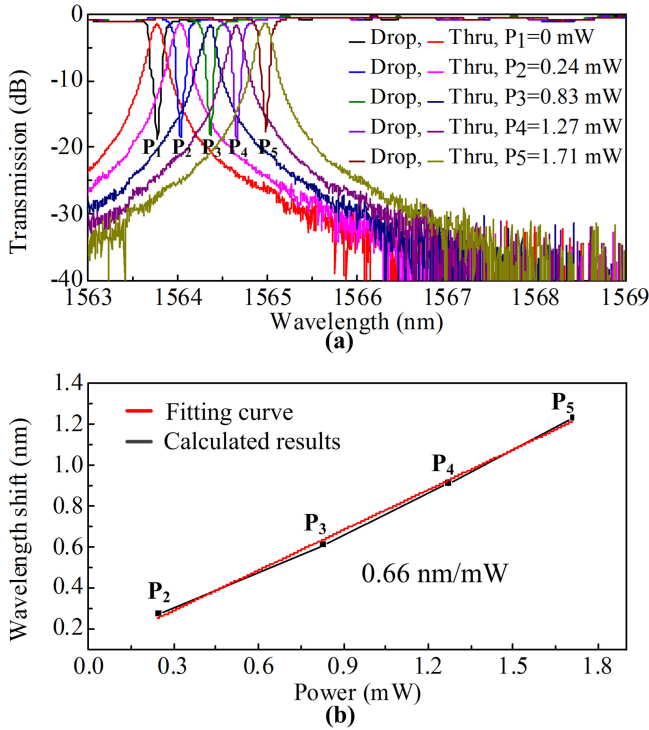
Fig. 9. (a) Transmission spectra of the fabricated switch at the drop port and the thru port with varied applying powers ($P_1, P_2, P_3, P_4, P_5$). (b) Fitting curve of the resonance wavelength shift versus the applied power.
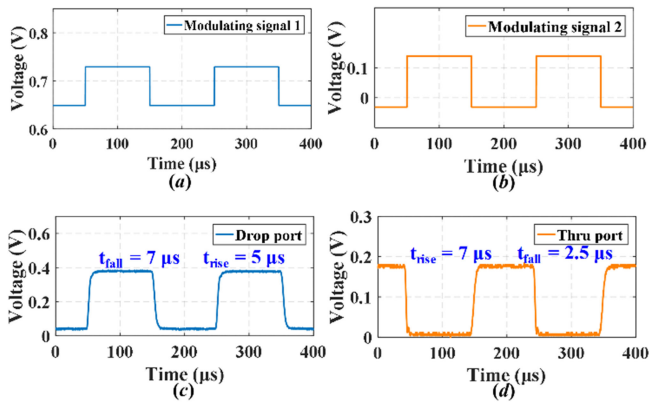


Fig. 10. Temporal responses of the switch. (a) The square-wave driving signal loaded onto the heater of PCN1. (b) The square-wave driving signal loaded onto the heater of PCN2. (c) The output signal from the drop port. (d) The output signal from the through port.

In order to measure the temporal responses of the switch, two 5-kHz square-wave electric signals were loaded onto the two heaters simultaneously, as shown in Fig. 10. The rise time and falling time of the modulating signals are ~9 ns. The input optical signal is a continuous wave. The results show a 10%−90% rising time of 5 $\mu$s and a 90%−10% falling time of 7 $\mu$s at the drop port, and a 10%−90% rising time of 7 $\mu$s and a 90%−10% falling time of 2.5 $\mu$s at the through port.

Table I compares our results versus other reports in literature. The device is advantageous in achieving a very low switching

TABLE I
CHARACTERISTICS OF INTEGRATED OPTICAL SWITCHES

| Type | Device Footprint | Switching Power (mW) | IL (dB) | Bandwidth (nm) | ER (dB) |
|---|---|---|---|---|---|
| Adiabatic bend-based MZI [29] | ~ 5000 $\mu m^2$ | 12.7 | 0.5 | 70 | 20 |
| Suspended MZI [30] | 1000 $\mu$m × 40 $\mu$m | 0.49 | 0.3 | — | 23 |
| Two-section DC EO MZI [31] | ~ 0.065 $mm^2$ | ~25 | 1.2 | 45 | 23 |
| EO nested MZI [32] | ~ 0.14 $mm^2$ | ~34 | 2 | 8 | 32.5 |
| Electrodes enhanced MZI [33] | 240 $\mu$m × 24 $\mu$m | 1.1 | 0.5 | ~100 | 11.5 |
| Dual cascaded MRRs [34] | ~1000 $\mu m^2$ | 6.0 | 4 | 0.2 | 20 |
| Ten coupled EO MRRs [35] | ~ 0.037 $mm^2$ | 37 | 4.3 | ~ 0.8 | 50 |
| 2D-Photonic crystal switch [20] | ~16.8 $\mu$m × 8 $\mu$m | 8.9 | 2.5 | ~ 1 | 23.5 |
| Photonic crystal microcavities [22] | ~ 35 $\mu$m × 10 $\mu$m | 18.2 | 1 | 6 | 20 |
| Three waveguide nanobeam MZI [23] | 30 $\mu$m × 150 $\mu$m | 0.16 | 1.5 | 0.09 | 15 |
| Polymer-based TO switch [36] | ~ 24000 $\mu$m × 50 $\mu$m | 5.2 | ~1.7 | — | 25.2 |
| Graphene-based fiber MZI [37] | ~ 120 $\mu$m × 40 $\mu$m | 5.3 | 1.2 | 0.4 | 19 |
| III-V/Si hybrid MOS* based MZI [38] | ~ 1300 $\mu$m × 200 $\mu$m | $0.18 \times 10^{-6}$ | ~1 | ~ 40 | 23 |
| This work | 75 $\mu$m × 15 $\mu$m | 0.24 | 1.5 | 0.12 | 15 |

MOS*: metal-oxide-semiconductor

power of 0.24 mW with a compact footprint of 15 $\mu$m × 75 $\mu$m. Together with Tab. 7 in [28], it can be seen that our results show a low power consumption and a small device footprint, while maintaining reasonable performances in crosstalk, insertion loss, and switching time. This is the smallest resonator based MZI switch with a submilliwatt TO switching power, to the best of our knowledge.

## IV. TWO-DIMENSIONAL SWITCHES

To increase the switching capacity, introducing more physical dimensions is an effective approach. Mode multiplexing, as an emerging signal processing technology in the spatial domain, has attracted tremendous interest. By combining with wavelength or polarization, two-dimensional switching can be realized. A pioneering work demonstrated on-chip optical interconnects with 2 spatial modes and 3 WDM channels [3], 10-Gb/s data signals were multiplexed, transmitted through the link, and de-multiplexed. More recently, WDM-compatible mode

multiplexing/de-multiplexing and switching were implemented with a full integration of modulators and photodetectors [39]. 25-Gb/s signals were used to demonstrate a 3-wavelength × 2-mode × 25-Gbps on-chip data throughput. A wavelength and mode selective switch was demonstrated with two wavelengths and two modes on a SOI wafer [40].

On the other hand, mode and polarization dimensions can be utilized to multiplex data channels with only one laser source, instead of multiple lasers in the WDM-MDM scenario. In this case, mode and polarization (de)multiplexers become essential components. Recently, we presented an on-chip 1 × 2 mode- and polarization-selective switch (MPSS) [41], and further developed it to a 2 × 2 MPSS device with low crosstalk [5]. Similar to a wavelength-selective switch (WSS), the MPSS can route any polarization/mode channel from one input port to any output port. With 2 input/output ports, 2 modes, 2 polarizations, and a 93.5-Gb/s data rate, 748-Gb/s switching capacity was demonstrated on a single wavelength [42].

To further scale the capacity, it is desired to combine the three physical dimensions to perform switching in wavelength, polarization and mode.

## V. THREE-DIMENSIONAL MODE-POLARIZATION-WAVELENGTH SELECTIVE SWITCH

In this section, we present a design of a switch in three dimensions of mode, polarization and wavelength. This is the first design of a three-dimensional switch, to the best of our knowledge. We also demonstrate the building blocks and key functionalities, and perform a proof-of-concept experiment of optical switching in three dimensions.

In analogy to a conventional 2 × 2 wavelength selective switch (WSS), this mode-polarization-wavelength selective switch (MPWSS) has two input ports and two output ports. However, the de-multiplexing and multiplexing are performed in three dimensions including mode, polarization and wavelength. For a mode and polarization switch, each channel is broadband. While for an MPWSS, wavelength demultiplexing and switching functions should be realized, which can be implemented by a wavelength add-drop filter as an example. Other conventional approaches, such as arrayed waveguide gratings + Mach-Zehnder switches [43], can be employed. Fig. 11 shows an on-chip 2 × 2 optical switching architecture for mode-, polarization- and wavelength-multiplexed signals based on the MRRs. The 2$K$-MDM, 2-PDM and $M$-WDM signals are injected into the photonic chip, then de-multiplexed to 2$K$ fundamental mode signals by mode de-multiplexers and polarization beam splitters (PBSs). Each signal is switched to an output port by a 1 × 2 MRR. The routed signals are combined by mode multiplexers and polarization beam combiners (PBCs) at the output. The wavelength multiplexing, switching, and wavelength de-multiplexing functions in Fig. 2 can be simultaneously realized by a tunable add-drop MRR. For a full implementation, the 2 × 2 MPWSS chip needs $K$ (modes) × 2 (polarizations) × $M$ (wavelengths) × 2 (ports) = 4$KM$ MRRs.

For a proof-of-concept experiment, we demonstrate one switching layer using tunable MRRs of the same wavelength
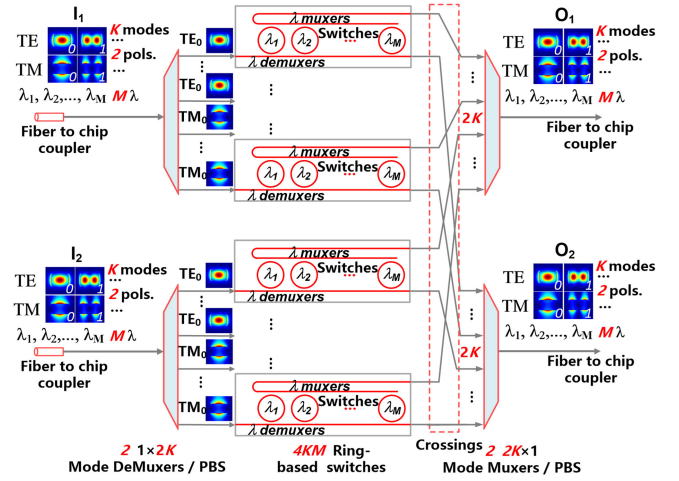


Fig. 11. On-chip optical switching network architecture for mode-, polarization- and wavelength- multiplexed signals based on ring switches.
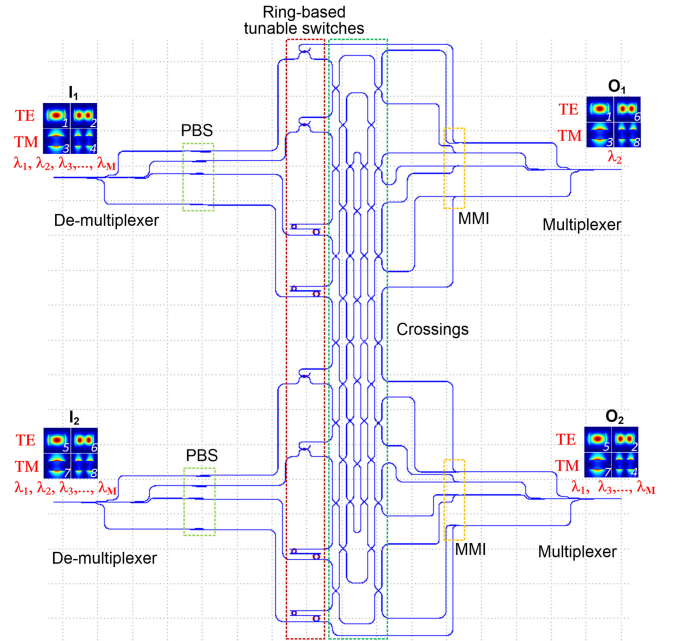


Fig. 12. Schematic configuration of the proposed silicon 2 × 2 MPWSS. As an example, the TE$_0$, $\lambda_2$ and TM$_0$, $\lambda_2$ channels of I$_1$ and the TE$_1$, $\lambda_2$ and TM$_1$, $\lambda_2$ channels of I$_2$ are routed to O$_1$, and other channels are routed to O$_2$.

to show the feasibility, instead of $M$ layers. The design layout of a 2 × 2 MPWSS chip is provided in Fig. 12, which requires 2 (modes) × 2 (polarizations) × 1 (wavelengths) × 2 (ports) = 8 tunable MRR switches operating on the same wavelength. Note that more MRRs can be cascaded and placed between the two bus waveguides for wavelength de-multiplexing and multiplexing as illustrated in Fig. 11, and each MRR switch corresponds to a wavelength layer. Therefore, the multi-layer topology in Fig. 2 becomes a one-layer physical implementation with the cascaded MRRs. The free spectral range (FSR) of an MRR may cover several wavelength channels, thus simplifying the device design.
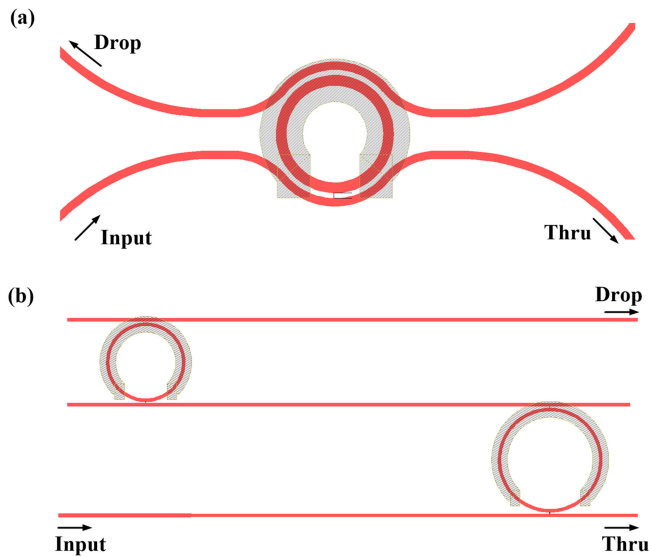
Fig. 13. (a) Structure of the single microring switch for the $TE_0$ polarization. (b) Vernier-filter switch for the $TM_0$ polarization.
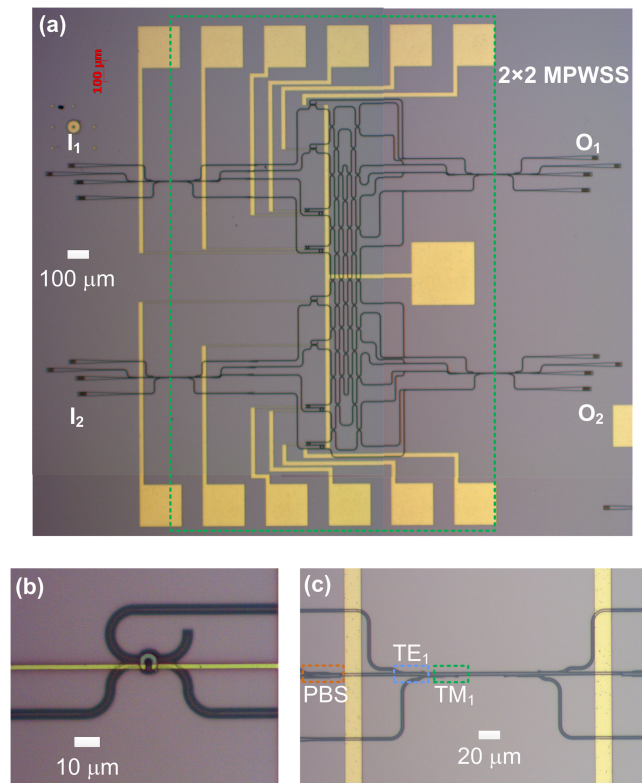


Fig. 14. (a) Microscope photo of a fabricated MPWSS chip. Magnified microscope photos of (b) tunable ring-based switches for $TE_0$ polarization, (c) PBS and mode multiplexers.

In details, two fundamental modes ($TE_0$ and $TM_0$) and two high-order modes ($TE_1$ and $TM_1$) are injected from the input port $I_1$ or $I_2$, and de-multiplexed into 4 fundamental mode channels by mode de-multiplexers and PBSs. Then, the signals are routed by the corresponding $TE_0$ or $TM_0$ tunable switches, multiplexed by the PBCs and the mode multiplexers, and then output from the port $O_1$ or $O_2$. Eight PBSs that function as polarization or mode filters, are cascaded to the mode de-multiplexers respectively to filter the undesired polarizations or modes and reduce the inter-modal crosstalk. Two PBSs and two PBCs are included in the demultiplexers and the multiplexers to split and combine the two orthogonal polarizations of TE and TM, respectively. In total, the proposed $2 \times 2$ MPWSS chip consists of 4 mode (de)multiplexers, 10 PBSs, 8 thermo-optic microring-based switches, 8 $1 \times 2$ multi-mode interferometer (MMI) couplers, 2 PBCs and 40 waveguide crossings. The structures and the design parameters of the mode multiplexers, PBSs, MMI couplers, PBCs and crossings can be found in [5]. Fig. 13 shows the structures of the tunable MRR switches. For the $TE_0$ single ring switch, the radius of the microring is 2.5 $\mu$m to achieve a large free spectral range (FSR) of >35 nm. The rectangular cross-section of the ring waveguide is 450 nm $\times$ 220 nm. The ring waveguide is side coupled to two bus waveguides using bent directional couplers with a gap of 305 nm and a coupling angle of 100°. The widths of the bus waveguides are reduced to 340 nm to achieve a better phase match between the ring waveguide and the bus waveguides. For the $TM_0$ channel, it is difficult to realize an MRR with a small radius, as the sharp bend leads to a high propagation loss for the TM polarization. Therefore, two MRRs are used as a 2rd-order Vernier filter for the $TM_0$ switch. The radii of the two microrings are 8 $\mu$m and 6 $\mu$m, respectively. The widths of the ring waveguide and the bus waveguide are both 450 nm. The gap between the ring and the bus waveguides of the 6-$\mu$m-radius ring and the 8-$\mu$m-radius ring are 275 nm and 305 nm, respectively. A metal heater with a width of 2 $\mu$m enables

the thermo-tuning of the MRR. The two microrings are placed 50 $\mu$m apart to reduce the thermal crosstalk.

EBL (Vistec EBPG 5200$^+$) and ICP etching process were used to define the MPWSS structures on a SOI wafer. A 2-$\mu$m-thick $SiO_2$ cladding was deposited using PECVD. 250-nm-thick Ti heaters and 300-nm-thick Au contact pads were formed by the lift-off process using E-beam evaporator. The microscope photos of a fabricated MPWSS chip are shown in Fig. 14. The footprint of the MPWSS device is less than 1.63 mm $\times$ 1.7 mm. In our measurements, grating couplers were used to couple the $TE_0$- and $TM_0$- polarized lights into/out of the chip. To couple the fundamental $TE_0$- and $TM_0$- polarized lights into and out of the chip using the grating couplers, mode (de)multiplexers are added to the input (output) ports of the MPWSS. A tunable continuous wave (CW) laser (Keysight 81960A) and an optical power meter were used to characterize the fabricated devices. The details of the measurement setup can be found in [5]. It should be noted that coupling between the multimode waveguides and the external few mode fibers are needed for practical applications.

We also fabricated individual PBSs, mode (de)multiplexers, crossings, $1 \times 2$ MMIs and MRRs on the same wafer and characterized the performances of these unit devices. The insertion losses of the building blocks are summarized in Table II.

Fig. 15 shows measured transmission spectra of the MPWSS device. The transmission spectra were normalized to that of the identical grating couplers and the mode (de)multiplexers for coupling and testing the MPWSS chip (outside of the green

TABLE II
MEASURED INSERTION LOSSES OF THE BUILDING BLOCKS

| Building block | Insertion loss (dB) |
|---|---|
| PBS for $TE_0$ | 0.78 |
| PBS for $TM_0$ | 2.8 |
| Mode (de)multiplexer for $TE_1$ | 0.86 |
| Mode (de)multiplexer for $TM_1$ | 1.68 |
| Crossing for $TE_0$ | 0.09 |
| Crossing for $TM_0$ | 0.12 |
| $1 \times 2$ MMI for $TE_0$ | 4.1 (port 1), 5.0 (port 2) |
| $1 \times 2$ MMI for $TM_0$ | 3.2 (port 1), 3.6 (port 2) |
| MRR of 2.5-$\mu$m radius for $TE_0$ | 2.7 (Thru port), 4.5 (Drop port) |
| MRR of 6-$\mu$m radius for $TM_0$ | 0.5 (Thru port), 2.5 (Drop port) |
| MRR of 8-$\mu$m radius for $TM_0$ | 0.8 (Thru port), 0.7 (Drop port) |
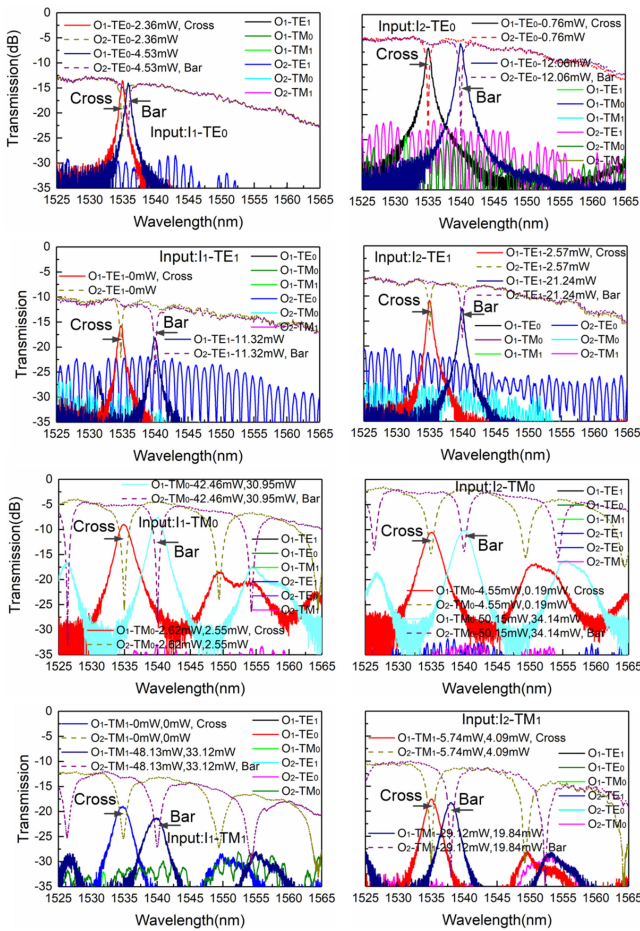


Fig. 15. Measured transmission spectra of the fabricated MPWSS chip including de-multiplexing, switching and multiplexing elements.

dash box), which were fabricated on the same chip. For this proof-of-concept experiment, only one signal wavelength on one switching layer is demonstrated, which locates at 1535 nm. The switches are at the cross states if their resonances are set to 1535 nm, whereas the switches change to the bar states if the resonances are shifted away from 1535 nm. Taking the $TE_0$ channel at input port $I_1$ as an example, the signal at

1535 nm is switched to output port $O_1$ when a heating power of 2.36 mW is applied, and the signal is routed to output port $O_2$ if the heating power increases to 4.53 mW. The $I_1$-$TE_0$ channel shows a narrower tuning range, due to the imperfection of the heater on the MRR. The insertion losses are lower than 12.8 dB, which are mainly caused by the scattering from the waveguide sidewalls, incomplete coupling in the mode multiplexer and the PBS, non-critical coupling of the microrings, and the 3-dB coupling loss of the MMI coupler. The inter-modal crosstalk values are below $-11.3$ dB. For the $I_1$-$TM_0$ channel input, the signal at 1535 nm is switched to output port $O_1$ when the heating powers on the 8-$\mu$m-radius ring and the 6-$\mu$m-radius ring are 2.62 mW and 2.55 mW, respectively. The signal is routed to output port $O_2$ when the applied heating powers are 42.46 mW and 30.95 mW, respectively. The insertion losses are lower than 9.4 dB and the inter-modal crosstalk values are below $-16.4$ dB. For all the other channels, optical signals on different polarization and mode channels can be independently routed to arbitrary output ports by applying different heating powers on the corresponding MRR switches. The total switching power for all the eight channels is 311.63 mW. For the TM channels, there are multiple notches in the wavelength range of 1525 nm $\sim$ 1565 nm, due to the small FSR values of the 8-$\mu$m-radius MRRs. The insertion loss of the MPWSS chip does not include the fiber-chip coupling losses. For the channels of $I_1$-$TE_0$ and $I_1$-$TE_1$, the insertion losses may be attributed to that of the $1 \times 2$ MMIs and non-critical coupling of the 2.5-$\mu$m-radius MRRs. Incomplete coupling of TM polarization in the PBSs and non-critical coupling of 6-$\mu$m-radius and 8-$\mu$m-radius MRRs lead to the high insertion losses for the channels of $I_1$-$TM_1$ and $I_2$-$TM_1$. The beating lengths of the $1 \times 2$ MMIs need to be optimized to reduce the insertion losses. The waveguide gaps of the MRRs and the coupling lengths of the PBSs can be engineered to achieve complete coupling and low losses. The bandwidths and the crosstalk performances of the switches may be improved by optimizing the design parameters and using cascaded MRRs. Significant performance improvement can be expected with more fabrications with iterative optimizations towards more practical implementations. Whereas in this paper we focus on demonstrating the basic functions of such a new on-chip MPWSS switch. Although only one wavelength layer is demonstrated, the MPWSS architecture is scalable in wavelength by cascading more MRRs. Both the mode and the wavelength (de)multiplexers use the bus waveguide structures, enabling good scalability towards high radix switching. In our previous study [15], an 11-channel mode (de)multiplexer was demonstrated with a maximal channel loss of 2.6 dB. For the MRR wavelength (de)multiplexer, the loss is almost independent on the number of channels.

VI. CONCLUSION

In this paper, we discussed a general architecture for optical switching in arbitrary physical dimensions including wavelength, mode, and polarization. We first demonstrated a $2 \times 2$ dual-nanobeam wavelength switch with a high Q-factor of 13000, a low TO switching power of 0.24 mW, and a compact

footprint of 15 $\mu$m $\times$ 75 $\mu$m. We then presented a design of a $2 \times 2$ MPWSS, and performed a proof-of-concept demonstration with 8 channels that consist of 2 modes, 2 polarizations, 1 wavelength and 2 input/output ports. The transmission spectra of all the channel combinations were measured, and the switching function was demonstrated. These demonstrations may provide potential solutions for future multi-dimensional, scalable, large capacity, and low power optical switches.

## ACKNOWLEDGMENT

## REFERENCES

[1] P. J. Winzer, D. T. Neilson, and A. R. Chraplyvy, "Fiber-optic transmission and networking: The previous 20 and the next 20 years," *Opt. Express*, vol. 26, no. 18, pp. 24190–24239, Sep. 2018.

[2] R. Ryf *et al.*, "32-bit/s/Hz spectral efficiency WDM transmission over 177-km few-mode fiber," in *Proc. Opt. Fiber Commun. Conf.*, 2013, Paper PDP5A.1.

[3] L. Luo *et al.*, "WDM-compatible mode-division multiplexing on a silicon chip," *Nature Commun.*, vol. 5, Jan. 2014, Art. no. 3069.

[4] B. Stern *et al.*, "On-chip mode-division multiplexing switch," *Optica*, vol. 2, no. 6, pp. 530–535, Jun. 2015.

[5] Y. Zhang, Y. He, Q. Zhu, C. Qiu, and Y. Su, "On-chip silicon photonic $2 \times 2$ mode-and polarization-selective switch with low inter-modal crosstalk," *Photon. Res.*, vol. 5, no. 5, pp. 521–526, Oct. 2017.

[6] Y. Su *et al.*, "Silicon photonic devices for optical switching in wavelength, polarization and mode," in *Proc. Opt. Fiber Commun. Conf.*, 2019, Paper W1E. 3.

[7] X. Jiang, H. Zhang, C. Qiu, Y. Zhang, Y. Su, and R. Soref, "Compact and power efficient $2 \times 2$ thermo-optical switch based on dual-nanobeam MZI," in *Proc. Opt. Fiber Commun. Conf.*, 2018, Paper Th2A.7.

[8] P. J. Winzer, "Making spatial multiplexing a reality," *Nature Photon.*, vol. 8, no. 5, pp. 345–348, Apr. 2014.

[9] L. Yang *et al.*, "General architectures for on-chip optical space and mode switching," *Optica*, vol. 5, no. 2, pp. 180–187, Feb. 2018.

[10] G. I. Papadimitriou, C. Papazoglou, and A. S. Pomportsis, "Optical switching: Switch fabrics, techniques, and architectures," *IEEE/OSA J. Lightw. Technol.*, vol. 21, no. 2, pp. 384–405, Feb. 2003.

[11] R. A. Jensen, "Optical switch architectures for emerging colorless/directionless/contentionless ROADM networks," in *Proc. Opt. Fiber Commun. Conf.*, 2011, Paper OThR.3.

[12] N. Farrington *et al.*, "Helios: A hybrid electrical/optical switch architecture for modular data centers," *SIGCOMM Comput. Commun. Rev.*, vol. 40, no. 4, pp. 339–350, Oct. 2010.

[13] B. Lee and N. Dupuis, "Silicon photonic switch fabrics: Technology and architecture," *IEEE/OSA J. Lightw. Technol.*, vol. 37, no. 1, pp. 6–20, Jan. 2019.

[14] N. K. Fontaine *et al.*, "530 $\times$ 30 MIMO transmission over 15 spatial modes," in *Proc. Opt. Fiber Commun. Conf.*, 2015, Paper PDP5C.1.

[15] Y. He *et al.*, "Silicon high-order mode (de)multiplexer on single polarization," *IEEE/OSA J. Lightw. Technol.*, vol. 36, no. 24, pp. 5746–5753, Dec. 2018.

[16] D. A. B. Miller, "Attojoule optoelectronics for low-energy information processing and communications," *IEEE/OSA J. Lightw. Technol.*, vol. 35, no. 3, pp. 346–396, Feb. 2017.

[17] R. Soref and J. Hendrickson, "Proposed ultralow-energy dual photonic-crystal nanobeam devices for on-chip N $\times$ N switching, logic, and wavelength multiplexing," *Opt. Express*, vol. 23, no. 25, pp. 32582–32596, Dec. 2015.

[18] X. C. Ge, Y. C. Shi, and S. L. He, "Ultra-compact channel drop filter based on photonic crystal nanobeam cavities utilizing a resonant tunneling effect," *Opt. Lett.*, vol. 39, no. 24, pp. 6973–6976, Dec. 2014.

[19] K. Nozaki *et al.*, "Sub-femtojoule all-optical switching using a photonic-crystal nanocavity," *Nature Photon.*, vol. 4, no. 7, pp. 477–483, May 2010.

[20] Z. Qiang *et al.*, "Compact thermo-optic switch based on tapered W1 photonic crystal waveguide," *IEEE Photon. J.*, vol. 5, no. 2, Apr. 2013, Art. no. 2200606.

[21] A. Shakoor, K. Nozaki, E. Kuramochi, K. Nishiguchi, A. Shinya, and M. Notomi, "Compact 1D-silicon photonic crystal electro-optic modulator operating with ultra-low switching voltage and energy," *Opt. Express*, vol. 22, no. 23, pp. 28623–28634, Nov. 2014.

[22] X. Zhang, S. Chakravarty, C. J. Chung, Z. Pan, Y. Hai, and R. T. Chen, "Ultra-compact and wide-spectrum-range thermo-optic switch based on silicon coupled photonic crystal microcavities," *Appl. Phys. Lett.*, vol. 107, no. 22, Nov. 2015, Art. no. 221104.

[23] H. Zhou *et al.*, "Compact, submilliwatt, $2 \times 2$ silicon thermo-optic switch based on photonic crystal nanobeam cavities," *Photon. Res.*, vol. 5, no. 2, pp. 108–112, Apr. 2017.

[24] W. S. Fegadolli, J. E. B. Oliveira, V. R. Almeida, and A. Scherer, "Compact and low power consumption tunable photonic crystal nanobeam cavity," *Opt. Express*, vol. 21, no. 3, pp. 3861–3871, Feb. 2013.

[25] C. V. Poulton, X. G. Zeng, M. T. Wade, J. M. Shainline, J. S. Orcutt, and M. A. Popovic, "Photonic crystal microcavities in a microelectronics 45-nm SOI CMOS technology," *IEEE Photon. Technol. Lett.*, vol. 27, no. 6, pp. 665–668, Jan. 2015.

[26] Q. M. Quan *et al.*, "Single particle detection in CMOS compatible photonic crystal nanobeam cavities," *Opt. Express*, vol. 21, no. 26, pp. 32225–32233, Dec. 2013.

[27] Q. M. Quan and M. Loncar, "Deterministic design of wavelength scale, ultra-high Q photonic crystal nanobeam cavities," *Opt. Express*, vol. 19, no. 19, pp. 18529–18542, Sep. 2011.

[28] Y. Li, Y. Zhang, L. Zhang, and A. W. Poon, "Silicon and hybrid silicon photonic devices for intra-datacenter applications: State of the art and perspectives," *Photon. Res.*, vol. 3, no. 5, pp. B10–B27, Oct. 2015.

[29] M. R. Watts, S. Jie, D. R. Christopher, D. C. Trotter, R. W. Young, and G. N. Nielson, "Adiabatic thermo-optic Mach–Zehnder switch," *Opt. Lett.*, vol. 38, no. 5, pp. 733–735, Mar. 2013.

[30] Q. Fang *et al.*, "Ultralow power silicon photonics thermo-optic switch with suspended phase arms," *IEEE Photon. Technol. Lett.*, vol. 23, no. 8, pp. 525–527, Apr. 2011.

[31] N. Dupuis *et al.*, "Design and fabrication of low-insertion-loss and low-crosstalk broadband $2 \times 2$ Mach–Zehnder silicon photonic switches," *IEEE/OSA J. Lightw. Technol.*, vol. 33, no. 17, pp. 3597–3606, Sep. 2015.

[32] N. Dupuis *et al.*, "Ultralow crosstalk nanosecond-scale nested $2 \times 2$ Mach–Zehnder silicon photonic switch," *Opt. Lett.*, vol. 41, no. 13, pp. 3002–3005, Jul. 2016.

[33] K. Chen, F. Duan, and Y. Yu, "Performance-enhanced silicon thermo-optic Mach–Zehnder switch using laterally supported suspended phase arms and efficient electrodes," *Opt. Lett.*, vol. 44, no. 4, pp. 951–954, Feb. 2019.

[34] P. Dong *et al.*, "Low power reconfigurable multiplexing devices based on silicon microring resonators," *Opt. Express*, vol. 18, no. 10, pp. 9852–9858, May 2010.

[35] X. Luo *et al.*, "Silicon high-order coupled-microring-based electrooptical switches for on-chip optical interconnects," *IEEE Photon. Technol. Lett.*, vol. 24, no. 10, pp. 821–823, May 2012.

[36] M. Jiang *et al.*, "Low power consumption thermo-optic switch formed by an integrated processing method," *Appl. Opt.*, vol. 58, no. 27, pp. 7375–7378, Sep. 2019.

[37] T. Hao, Z. Chang, and K. Chiang, "Externally pumped low-loss graphene-based fiber Mach–Zehnder all-optical switches with mW switching powers," *Opt. Express*, vol. 27, no. 4, pp. 4216–4225, Feb. 2019.

[38] Q. Li, J. Han, C. Ho, S. Takagi, and M. Takenaka, "Ultra-power-efficient $2 \times 2$ Si Mach–Zehnder interferometer optical switch based on III-V/Si hybrid MOS phase shifter," *Opt. Express*, vol. 26, no. 26, pp. 35003–35012, Dec. 2018.

[39] H. Jia *et al.*, "WDM-compatible multimode optical switching system-on-chip," *Nanophotonics*, vol. 8, no. 5, pp. 889–898, May 2019.

[40] L. Han, B. P. Kuo, N. Alic, and S. Radic, "Silicon photonic wavelength and mode selective switch for WDM-MDM networks," in *Proc. Opt. Fiber Commun. Conf.*, 2019, Paper M3B.4.

[41] Y. Zhang, Q. Zhu, Y. He, C. Qiu, Y. Su, and R. Soref, "Silicon $1 \times 2$ mode- and polarization-selective switch," in *Proc. Opt. Fiber Commun. Conf.*, 2017, Paper W4E.2.

[42] Q. Zhu *et al.*, "On-chip switching of mode- and polarization-multiplexed signals with a 748-Gb/s/$\lambda$ ($8 \times 93.5$-Gb/s) capacity," in *Proc. Conf. Laser Electro-Opt.*, 2018, Paper SW4C.2.

[43] S. Wang, H. Wu, H. K. Tsang, and D. Dai, "Monolithically integrated reconfigurable add-drop multiplexer for mode-division-multiplexing systems," *Opt. Lett.*, vol. 41, no. 22, pp. 5298–5301, Nov. 2016.

**Yong Zhang** (M'16) received the B.S. degree from Northwestern Polytechnical University, Xi'an, China, in 2010, and the Ph.D. degree from the Huazhong University of Science and Technology, Wuhan, China, in 2015. In 2015, he joined Shanghai Jiao Tong University, Shanghai, China, as an Assistant Professor and became an Associate Professor in 2019. He has authored or coauthored more than 60 journal and conference papers, including the JOURNAL OF LIGHTWAVE TECHNOLOGY, *Advanced Optical Materials*, *Optics Letters*, OFC/ECOC/CLEO, etc. His research interests include silicon photonics devices, polarization and mode devices, microcavity devices, e-beam lithography, and ICP etching process.

Dr. Zhang was an Editorial Board Member of the Journal of Semiconductors and a Guest Editor for *Science China Information Sciences* (2017). He was the Secretary (2016–2017) and is the Treasurer (2017–) of the IEEE Photonics Society Shanghai Chapter. He was also a TPC member of several international conferences. He is a Member of The Optical Society.

**Ruihuan Zhang** received the B.S. and M.S. degrees from the Harbin Institute of Technology, Harbin, China, in 2015 and 2017, respectively. She is currently working toward the Ph.D. degree at Shanghai Jiao Tong University, Shanghai, China. Her research interests include silicon photonics and low-power optical switches.

**Qingming Zhu** received the B.S. degree from Southeast University, Nanjing, China, in 2015. He is currently working toward the Ph.D. degree at Shanghai Jiao Tong University, Shanghai, China. His research interests include silicon microring switches and high-speed transmission systems.

**Yuan Yuan** received the B.S. degree from the Xi'an University of Posts and Telecommunications, Xi'an, China, in 2017. She is currently working toward the M.S. degree at Shanghai Jiao Tong University, Shanghai, China. Her research interests include low-power and small-mode volume optical switches.

**Yikai Su** (M'01–SM'07) received the Ph.D. degree in EE from Northwestern University, Evanston, IL, USA, in 2001. He was a Member of Technical Staff with Crawford Hill Laboratory of Bell Laboratories, Crawford, NJ, USA. In 2004, he joined Shanghai Jiao Tong University as a Full Professor. He has more than 400 publications in international journals and conferences, with more than 4300 citations (scopus search). He holds six U.S. patents and nearly 50 Chinese patents. His research areas cover silicon photonic devices, optical transmission, and switching.

Prof. Su was a Topical Editor for *Optics Letters* (2008–2014), a Guest Editor for the IEEE JOURNAL OF SELECTED TOPICS IN QUANTUM ELECTRONICS (2008/2011), and is an Associate Editor for *APL Photonics* (2016–). He is the Chair of the IEEE Photonics Society Shanghai Chapter, a General Co-Chair of ACP 2012, and a TPC Co-Chair of ACP 2011 and APCC 2009. He was also a TPC member of a large number of international conferences including CLEO (2016–2018), ECOC (2013–2017), OFC (2011–2013, 2020–), OECC 2008, and LEOS (2005–2007).